Received: 3 May 2022 | Revised: 12 September 2022 | Accepted: 17 September 2022

DOI: 10.1002/hbm.26102

RESEARCH ARTICLE

WILEY

Combining sodium MRI, proton MR spectroscopic imaging, and intracerebral EEG in epilepsy

Mikhael Azilinon[1,2,3] | Julia Makhalova[3,4] | Wafaa Zaaraoui[1,3] | Samuel Medina Villalon[2,4] | Patrick Viout[1,3] | Tangi Roussel[1,3] | Mohamed M. El Mendili[1,3] | Ben Ridley[5] | Jean-Philippe Ranjeva[1,3] | Fabrice Bartolomei[2,4] | Viktor Jirsa[2] | Maxime Guye[1,3]

[1]Aix Marseille Univ, CNRS, CRMBM, Marseille, France

[2]Aix Marseille Univ, INSERM, INS, Inst Neurosci Syst, Marseille, France

[3]APHM, Timone Hospital, CEMEREM, Marseille, France

[4]Epileptology Department, APHM, Timone Hospital, Marseille, France

[5]IRCCS Istituto delle Scienze Neurologiche di Bologna, Bologna, Italy

Correspondence
Maxime Guye, Centre de Résonance Magnétique Biologique et Médicale, Faculté des Sciences Médicales et paramédicales, 27, Bd Jean Moulin, 13385 Marseille Cedex 5, France.
Email: maxime.guye@univ-amu.fr

Funding information
"Programme Investissements d'Avenir", Excellence Initiative of Aix-Marseille University - A*MIDEX, Grant/Award Number: AMX-19IET-004; 7TEAMS Chair, EPINOV, Grant/Award Numbers: ANR-17-EURE-0029, ANR-17-RHUS-0004; Horizon 2020 Framework Program, Grant/Award Numbers: 785907, 945539

Abstract

Whole brain ionic and metabolic imaging has potential as a powerful tool for the characterization of brain diseases. We combined sodium MRI (^{23}Na MRI) and ^{1}H-MR Spectroscopic Imaging (^{1}H-MRSI), assessing changes within epileptogenic networks in comparison with electrophysiologically normal networks as defined by stereotactic EEG (SEEG) recordings analysis. We applied a multi-echo density adapted 3D projection reconstruction pulse sequence at 7 T (^{23}Na-MRI) and a 3D echo-planar spectroscopic imaging sequence at 3 T (^{1}H-MRSI) in 19 patients suffering from drug-resistant focal epilepsy who underwent presurgical SEEG. We investigated ^{23}Na MRI parameters including total sodium concentration (TSC) and the sodium signal fraction associated with the short component of T_2^* decay (*f*), alongside the level of metabolites N-acetyl aspartate (NAA), choline compounds (Cho), and total creatine (tCr). All measures were extracted from spherical regions of interest (ROIs) centered between two adjacent SEEG electrode contacts and *z*-scored against the same ROI in controls. Group comparison showed a significant increase in *f* only in the epileptogenic zone (EZ) compared to controls and compared to patients' propagation zone (PZ) and non-involved zone (NIZ). TSC was significantly increased in all patients' regions compared to controls. Conversely, NAA levels were significantly lower in patients compared to controls, and lower in the EZ compared to PZ and NIZ. Multiple regression analyzing the relationship between sodium and metabolites levels revealed significant relations

Abbreviations: ^{18}F-FDG-PET, fluorodeoxyglucose PET; ^{1}H, hydrogen; ^{23}Na, sodium; AC-PC, anterior commissure—posterior commissure; ASL, achieved significance level; Cho, choline compounds; CRLB, Cramer–Rao lower bound; DNET, dysembryoplastic neuroepithelial tumor; EAAT, glutamate transporter; ECV, extracellular volume; EI, Epileptogenicity Index; EPSI, echo-planar spectroscopic imaging; EZ, epileptogenic zone; f, fraction of sodium signal with short T_2^* decays; FCD, focal cortical dysplasia; FDR, false discovery rate; FOV, field of view; GRAPPA, GeneRalized Autocalibrating Partial Parallel Acquisition; HC, healthy control; MIDAS, Metabolite Imaging and Data Analyses System; MNI, Montreal Neurological Institute; MP2RAGE, magnetization prepared 2 rapid acquisition gradient echo; MPRAGE, magnetization prepared rapid acquisition gradient echo; Na+/K+ pump, sodium potassium pump; NAA, N-acetyl aspartate; Na_{LF}, apparent concentrations of sodium with long T_2^* decays; Na_{SF}, apparent concentrations of sodium with short apparent T_2^* decay; NBC, bicarbonate sodium cotransporter; NCX, sodium calcium exchanger; NHE, sodium hydrogen antiporter; NIZ, noninvolved zone; NKCC1, sodium potassium chloride cotransporter; pH, potential of hydrogen; PZ, propagation zone; QED, quality electrodynamics; ROI, region of interest; SEEG, stereotactic EEG; $T_2^*_{long}$, sodium longT_2^* relaxation time; $T_2^*_{short}$, sodium short T_2^* relaxation time; tCr, total creatine; TE, echo time; TI, inversion time; TR, repetition time; TSC, total sodium concentration; UTE, ultrashort echo time; VGNC, voltage-gated sodium channel.

in PZ and in NIZ but not in EZ. Our results are in agreement with the energetic failure hypothesis in epileptic regions associated with widespread tissue reorganization.

KEYWORDS
^{1}H-spectroscopic imaging, 7 T MRI, epilepsy, intracranial EEG, multimodal imaging, sodium MRI

1 | INTRODUCTION

Recent advances in neuroimaging have challenged the concept of focal epilepsy as a brain disorder strictly limited to the regions responsible for seizure generation and propagation (Larivière et al., 2021). Various MRI modalities (i.e., structural, functional, and metabolic) have consistently demonstrated structural and functional alterations that extend beyond the epileptogenic regions and affect areas noninvolved in ictal discharges or interictal epileptiform activity. These complex changes affect both structure and function at different spatial and temporal scales and can reflect seizure-induced alterations, neuronal plasticity as well as the underlying etiology. These factors, and the precise anatomical location of generators of epileptiform activity, are subject to variation even between individuals with the same epileptic syndrome. Thus, a systematic comparison of imaging data with the gold standard of electrophysiological data derived from intracerebral stereoelectroencephalography (SEEG) recording is essential to test the potential contribution of any imaging modality toward better definition of the epileptogenic zone (EZ) in patients suffering from drug-resistant focal epilepsy who are candidates for surgery. Moreover, the need to characterize the variable manifestations of pathology suggests a clear need to exploit multimodal imaging, combining metrics from different modalities. Insight into alterations of ionic homeostasis and metabolic function can be probed by sodium (^{23}Na) MRI and ^{1}H-MR spectroscopic imaging (MRSI), respectively.

^{23}Na-MRI provides a unique opportunity to noninvasively image sodium signal in the brain (Madelin et al., 2014). To date, the only ^{23}Na-MRI study performed in a group of human focal epilepsy, has demonstrated an increase of the total sodium concentration (TSC) in patients' brain compared to controls, which was greater in the EZ compared to the propagation zone (PZ) and the noninvolved regions (NIZs) (Ridley, Marchi, et al., 2017). The usefulness of TSC as a potential epileptogenicity marker may remain limited due to its limited specificity, as it likely reflects different underlying phenomena at the cellular level, such as changes in intracellular sodium concentration, changes in extracellular volume (ECV) and cell density and/or organization, among others.

For ^{23}Na-MRI, the increase in signal to noise available at 7 T allows novel approach based on a 3D-multi-echoes density-adapted radial sequence which exploits the biexponential T_2^* decay of the ^{23}Na MR signal (Ridley et al., 2018). This approach permits a multiparametric investigation of variation in T_2^* decay behavior related to the quadrupolar interactions of the 3/2 spin of ^{23}Na with the electric field gradient of surrounding molecules (Rooney & Springer, 1991), as an indicator of tissue organization and molecular environment. The biexponential fit model can be used as a probe to determine the motional regimes of sodium nuclei within the surrounding environment. Thus, by quantifying the sodium signal fraction with the short T_2^* decay component (f) this approach may offer a more relevant metric for studying tissue alterations and potentially provide a better link between sodium homeostasis and neuronal excitability in human epilepsy. In the present study, we implemented this multiparametric approach of sodium MRI for the first time in the assessment of profiles within and outside the epileptogenic and propagation networks in focal drug-resistant epilepsy.

As a further objective, we assessed metabolic alterations accompanying sodium concentration changes. To do so, we explored metabolic status by using whole-brain ^{1}H-Echo Planar spectroscopic imaging (^{1}H-EPSI) in the same subjects at 3 T. Three main metabolites were quantified: (i) N-acetyl aspartate (NAA) reflecting neuronal viability, mitochondrial dysfunction or neuronal loss (Moffett et al., 2013; Stefano et al., 1995), (ii) choline compounds (Cho) reflecting membrane turnover and inflammatory processes (Achten, 1998; Urenjak et al., 1993), and (iii) total-creatine compounds (tCr) reflecting intracellular energy states, and energy-dependent systems in the brain (Kreis et al., 1992; Kreis & Ross, 1992), and considered as a cellularity index (Kreis et al., 1993). Importantly, NAA has been consistently shown to be decreased in the epileptic brain, particularly in the EZ and PZ, compared to NIZs, and is thus considered as a potential epileptogenicity marker in focal epilepsy (Guye et al., 2002, 2005; Hugg et al., 1993; Kuzniecky et al., 1998; Lundbom et al., 2001; Simister et al., 2002). Furthermore, it has been hypothesized that the observed increase in TSC would mainly reflect energetic failures due to mitochondrial dysfunction affecting the Na^+/K^+ pump activity (Ridley, Marchi, et al., 2017; Stys et al., 1992). Thus, measuring both sodium and NAA in the same regions provides clues with regard to the mitochondrial defect hypothesis (Donadieu et al., 2019; Paling et al., 2011). However, the use of this metabolite has been limited by poor resolution and spatial coverage of routinely performed ^{1}H-MRSI, as well as by its insufficient specificity. In this study, we benefited from the whole brain coverage with a relatively high spatial resolution allowing comparison between multimodal MRI and electrophysiological metrics.

Therefore, through this trimodal approach, we aimed to characterize ionic and metabolic changes within epileptogenic networks in comparison with electrophysiologically normal appearing brain networks. For this purpose, we analyzed differences in ^{23}Na-MRI (TSC and f) and ^{1}H-MRSI (Cho, NAA, and tCr) metrics between patients and controls as well as between regions of interest (ROIs) defined by quantitative SEEG signal analysis (Figure 1). We then investigated the association between ^{23}Na-MRI and ^{1}H-MRSI metrics in EZ, PZ, and NIZ to link the homeostatic and metabolic mechanisms to the SEEG-recorded electrical alterations.

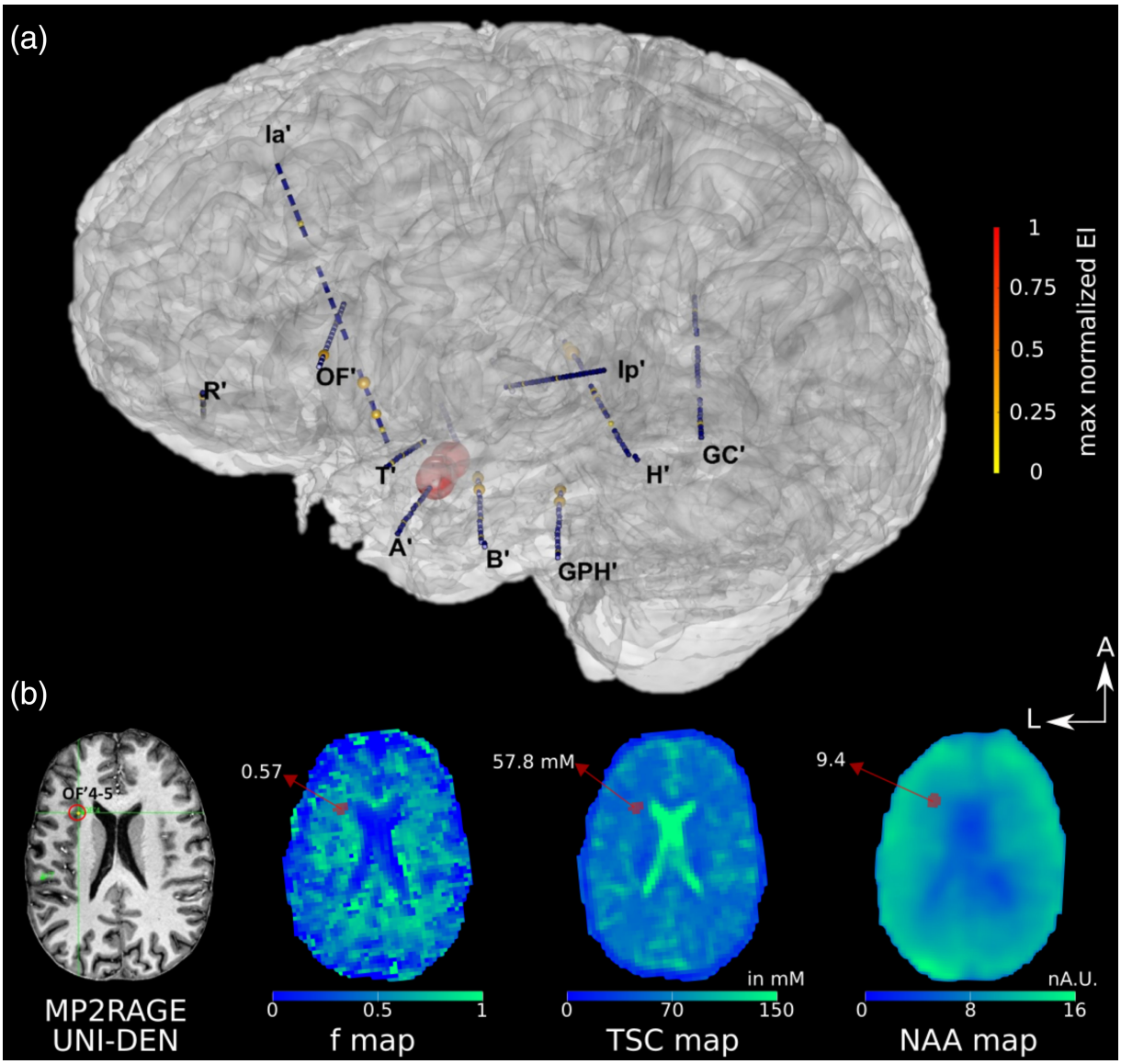

FIGURE 1 Illustrative case showing ROI selection for sodium MRI measures guided by quantified signal analysis of ictal intracerebral stereotactic EEG (SEEG) recordings. (a) Patient's 3D brain mesh (left hemisphere) with implanted SEEG electrodes. Reconstructed electrode images (blue) correspond to real trajectories and entry points (EpiTools software suite; Medina Villalon et al., 2018). The maximal Epileptogenicity Index (EI; Bartolomei et al., 2008) values are represented as spheres on the respective contacts according to a color map from yellow to red. Sphere size is proportional to the normalized EI value of the contact (from 0 to 1). The EI shows maximal epileptogenicity within the left amygdala, which belongs to the epileptogenic zone (EZ; EI ≥ 0.4), the left hippocampus, the parahippocampal cortex, the anterior insula, and the left pulvinar belong to the PZ (0.1 ≤ EI <0.4), whereas the remaining regions with available sampling belong to the NIZ (EI <0.1). Bipolar contacts situated entirely within the white matter or within the CSF (as defined by automated segmentation) or showing an artifact SEEG signal (visually checked) were excluded from the analysis. The ROIs obtained from the SEEG-analysis data sets were then used for multimodal imaging measures. (b) Axial slices of T_1w image, *f*, TSC, and NAA maps of the same patient. The ROI corresponding to the bipolar electrode contacts OF'4–5 (the left anterior insula, yellow dot circled in red on the T_1w slice) is represented as the red dot on the f, TSC, and NAA maps. Red arrows are pointing to the mean ROI value for each map.

2 | MATERIALS AND METHODS

2.1 | Subjects

Among all patients who underwent stereotactic intracerebral EEG (SEEG) recording in the context of presurgical evaluation for drug-resistant focal epilepsy at our center between January 2017 and February 19 2020 consecutive patients with available 3D ^{1}H-MRSI and ^{23}Na-MRI were retrospectively included (Table 1). All patients had detailed non-invasive presurgical evaluation including medical history, neurological examination, neuropsychological assessment, ^{18}F-FDG-PET, high-resolution structural 7 T and 3 T MRI, and a long-term scalp-video-EEG. All these steps were necessary for patient enrollment. The SEEG was indicated in all patients to localize the EZ and to

TABLE 1 Patient clinical demography

Patient	Gender	Age at epilepsy onset (years)	Epilepsy duration (years)	Seizure frequency (per month)	Epilepsy type	Side	3 T/7 T anatomical MRI	Surgical procedure	Engel class	Histology	^{23}Na-MRI/^{1}H-MRSI
1	F	10	14	2	Temporal latero-mesial	L	Normal	TC, SR	II	FCD1	Both
2	F	30	26	20	Temporo-parietal mesial	R	R posterior cingular FCD	TC, VNS, contra-indication for SR	NA	NA	Both
3	M	13	31	2	Insulo-parietal	L	Normal	TC, VNS contra-indication for SR	NA	NA	Both
4	F	24	9	4	Temporal mesial	R	Normal	TC, SR (ATL)	I	FCD3a	Both
5	F	10	27	3	Temporo-insular	L	Normal	TC, SR	I	FCD1	Both
6	M	3	26	120	Temporal mesial	L	Normal	TC, SR	II	slight gliosis	Both
7	M	12	11	8	Temporal mesial	L	Normal	TC, SR	II	FCD1b	Both
8	M	9	12	4	Temporo-insular	L	Normal	TC, contra-indication for SR	NA	NA	Both
9	M	2.5	24	10	Temporal lateral	L	Normal	TC, SR	III	slight gliosis	Both
10	F	40	9	30	Temporal mesial	R	Normal	TC, SR (ATL)	I	FCD1	Both
11	F	0.1	29	60	Orbitofronto-insular	L	L orbitofrontal FCD	TC, SR	III	FCD2a	Both
12	F	22	10	30	L parietal mesial, Bilateral temporal mesial	R&L	L posterior cingular NDT	TC, LITT (aiming NDT)	III	NA	Both
13	F	4	18	100	Bilateral temporal mesial, R insulo-operculo-frontal	R > L	Normal	TC, contra-indication for SR	NA	NA	Both
14	M	11	4	5	Temporal latero-mesial	L	Normal	TC, SR	I	FCD2a	^{23}Na-MRI
15	F	5	47	12	Temporo-parietal	L	L perisylvian PMG, schizencephaly, temporo-parietal PNH, R posterior PNH	TC, contra-indication for SR	NA	NA	^{1}H-MRSI
16	M	3	26	12	Temporal mesial	L	Normal	TC, patient refused SR	NA	NA	^{1}H-MRSI
17	F	17	10	5	Bilateral temporal mesial	R&L	Normal	TC, DBS, contra-indication for SR	NA	NA	Both
18	M	7	10	12	Insulo-opercular	L	Normal	TC, seizure free	NA	NA	Both
19	M	29	7	60	Temporal mesial	R	Normal	TC, SR (ATL)	III	FCD1c	Both

Abbreviations: ATL, anterior temporal lobectomy; DBS, deep brain stimulation; DNET, dysembryoplastic neuroepithelial tumor; FCD, focal cortical dysplasia; L, left; LITT, laser-guided interstitial thermal therapy; NA, not applicable; NDT, neuro-developmental tumor; PMG, polymicrogyria; PNH, periventricular nodular heterotopia; R, right; SR, surgical resection; TC, thermocoagulation; VNS, vagus nerve stimulation.

precisely determine its relation with eloquent areas. SEEG was performed as a part of the routine clinical management in line with the French national guidelines on stereoelectroencephalography (SEEG) (Isnard et al., 2018). SEEG implantation was planned individually for each patient, according to anatomo-electro-clinical hypotheses about the localization of the EZ based on noninvasive investigations. All SEEG explorations were bilateral and systematically sampled temporal, insular, frontal, and parietal regions of at least one hemisphere. Follow-up information was collected from a review of the medical records.

MRI data were always acquired before SEEG implantation. After quality checks (see below), 17 ^{1}H-MRSI data sets, and 15 ^{23}Na-MRI data sets of patients were used for further analysis. Thirteen out of the 19 patients fulfilled data quality in sufficient ROIs for both modalities. For ^{1}H-MRSI, we used a control database of 25 healthy controls (HCs; mean age 30.5 ± 9.7 years, range 20–60 years, 14 women). For ^{23}Na-MRI, we used a control database of 18 HCs (mean age 30.5 ± 8.36 years, range 21–54 years, 10 women). Participants provided informed consent in compliance with the ethical requirements of the Declaration of Helsinki and the protocol was approved by the local Ethics Committee (Comité de Protection des Personnes sud Méditerranée 1). ^{1}H-MRSI and ^{23}Na-MRI data sets were not part of the clinical evaluation and did not affect the clinical decision.

2.2 | MRI acquisitions

The protocol was conducted for all subjects on the two same MR scanners; the spectroscopic imaging protocol on a 3-Tesla Magnetom Verio MR system (Siemens) and the ^{23}Na MRI protocol on a whole-body 7-Tesla Magnetom Step 2 MR system (Siemens).

At 3 T, ^{1}H-MRI and ^{1}H-EPSI were performed with a 32 channel phased-array head coil and included a sagittal high-resolution 3D-MPRAGE protocol (TE/TR/TI = 3/2300/900 ms, 160 sections, 256 × 256 mm^2, FOV 256 × 256 matrix, resolution = 1 mm^3). Whole brain 3D ^{1}H-EPSI was acquired as described in Lecocq et al. (2015) using two axial acquisitions with two different orientations that are the AC-PC plane and the AC-PC + 15° plane (TE/TR/TI = 20/1710/198 ms, nominal voxel size = 5.6 × 5.6 × 10 mm^3, FOV = 280 × 280 × 180 mm^3, flip angle = 73°, 50 × 50 × 18k-space points, GeneRalized Autocalibrating Partial Parallel Acquisition (GRAPPA) factor = 2, acquisition time ≈ 17 min). The two angles of EPSI orientations were chosen to obtain good quality spectra on as large brain area as possible on at least one acquisition with a reasonable angulation to permit accurate automatic normalization procedure.

At 7 T, a high-resolution proton MRI 3D-MP2RAGE (TR = 5000 ms/TE = 3 ms/TI1 = 900 ms/TI2 = 2750 ms, 256 slices, 0.6 mm isotropic resolution, acquisition time = 10 min) was obtained using a 32-element (32Rx/1Tx) ^{1}H head coil (Nova Medical). ^{23}Na-MRI was acquired using a dual-tuned ^{23}Na/^{1}H QED birdcage coil and a multi-echo density adapted 3D projection reconstruction pulse sequence (TR = 120 ms, 5000 spokes, 384 radial samples per spoke, 3 mm nominal isotropic resolution, 24 echoes (8 per run with 3 runs, acquisition time 10 min per run; 30 min in total)). Three dimension ^{23}Na MRI volumes were obtained at 24 different TEs ranging from 0.2 to 70.78 ms (Run 1: 0.2–9.7–19.2–28.7–38.2–47.7–57.2–66.7 ms; Run 2: 1.56–11.06–20.56–30.06–39.56–49.06–58.56–68.06 ms; Run 3: 4.28–13.78–23.28–32.78–42.28–51.78–61.28–70.78 ms). This ensured a sufficient number and distribution of TEs while taking into account the 5 ms readout of the sequence, especially for measuring ^{23}Na signal with short T_2*. For quantitative calibration of brain sodium concentrations we used as external reference six tubes (80 mm length, 15 mm diameter) filled with a mixture of 2% agar gel and sodium at different concentrations: two tubes at 25 mM, one at 50 mM, two at 75 mM, and one at 100 mM. Tubes were positioned in the field of view in front of the subject's head and maintained using a cap.

2.3 | MRI data processing

Three dimension ^{1}H-EPSI images were post-processed with the Metabolite Imaging and Data Analyses System (MIDAS, Trac, MRIR, Miami; Maudsley et al., 2006). This software ensures B_0 map correction, lipid suppression, tissue volume fraction through T_1 segmentation, spectral fitting, exclusion of outlier voxels based on Cramer Rao lower bounds (CRLB), and signal normalization with the interleaved water signal acquired. MIDAS provided AC-PC and AC-PC 15° oriented maps, including metabolite maps (NAA, Cho, and tCr), quality maps, CRLB maps, and linewidth maps, among others that were used in further processing and quality check steps. In this study, we only analyzed NAA, tCr, and Cho maps because m-Ino (Myo-Inositol) and Glx (for glutamate, glutamine, and glutathione) maps did not fulfill CRLB criteria in the majority of the ROIs (Figure 2). ROI selection process is detailed in the next paragraph. The maps that we used for the ROIs signal extraction are the average maps of realigned AC-PC and AC-PC 15° oriented maps (Donadieu et al., 2019; Lecocq et al., 2015) (SPM12; Statistical Parametric Mapping: The Analysis of Functional Brain Images – 1st Edition, n.d.).

Metabolic profiles of each ROI (for details on ROI definition, see Section 2.6) were determined by extracting water signal normalized values (arbitrary unit) from corrected quantitative NAA, tCr, and Cho maps derived from MIDAS . We applied quality assurance criteria for spectra in each ROI based on a combination of Cramer-Rao minimum variance bound (CRLB < 15%, or CRLB lower than half of all HC), and water peak linewidth (<16 Hz) thresholds. Figure S1 illustrates the spectra that are in the permitted range or not. If, after ROIs rejection in a patient, there was no ROI in EZ, the patient was entirely discarded from further analyzes.

The ^{23}Na-MRI data were processed according to Grimaldi et al. (2021) using a homemade adjusted procedure. After brain extraction on ^{23}Na-MRI images (ANTS; Avants et al., 2011), a denoising filter was applied to the resulting ^{23}Na-MRI volumes (Aja-Fernandez et al., 2008; Rajan et al., 2010). The first echo time (TE) volumes from ^{23}Na MRI were used as reference for coregistration of the other TE volumes to correct for potential motion between acquisitions. Hand-drawn ROIs were placed in the center of each agar tube to extract

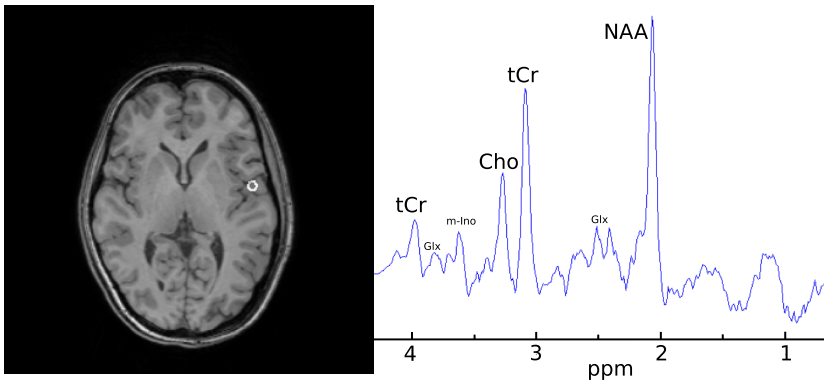

FIGURE 2 Spectrogram from a healthy control cortical voxel. Here, we highlighted the three metabolites we focused on in this study, namely total choline (Cho), N-acetyl aspartate (NAA), and total creatine (tCr). Glx, glutamate, glutamine, and glutathione; m-Ino, myo-Inositol.

signal intensities from the 24 TE volumes of ^{23}Na-MRI acquisitions for signal calibration procedure. Linear fitting of ^{23}Na signal decay from tubes ROI provided the slope (a) and intercept (b), which is used for calibration purposes (see below).

For each ROI (for details on ROI definition, see Section 2.6), we fitted the mean signal intensity across each of the 24 TEs with a biexponential model using the equation:

$$ROI\ signal = \sqrt{\left[A^2\left(f\cdot e^{\frac{-TE}{T2^*_{short}}} + (1-f)\cdot e^{\frac{-TE}{T2^*_{long}}}\right)^2 + Ric^2\right]} \quad (1)$$

where A is an amplitude scaling term, f is the sodium signal fraction of the short T_2* decay component, and *Ric* refers to a Rician noise-related scaling parameter (Ridley, Marchi, et al., 2017). From the model, we estimated a sodium signal fraction for short (f) and long ($1-f$) T_2* decay. Note that these short and long fractions of the sodium signal are only present when the Na^+ ions are present in an organized nonisotropic molecular environment. Indeed, in these environments, the electric quadrupolar moment of the sodium nucleus interacts strongly with the surrounding electric field gradient leading to a residual quadrupolar interaction responsible for the bi-exponential T_2 relaxation with a short T_2* and a long T_2* depending on the motional regime of the environment. In contrast, in an isotropic nonrestricted environment such as the cerebrospinal fluid, there is no residual quadrupolar interaction, and all energetic transitions are equal and lead to a monoexponential decay with only one (long) T_2* (Rooney & Springer, 1991). We calculated magnetization (M0) corresponding to the signal fraction estimated by the model in terms of the intercepts of the signal fraction components of the model, obtaining $M0_{SF} = A{\cdot}f$ and $M0_{LF} = A{\cdot}(1-f)$. Then, Na_{SF} and Na_{LF} were calculated with raw M0 signal values and the linear fit was estimated over the tube phantoms, that is, slope (a) and intercept (b):

$$Na_{SF} = \frac{(M0_{SF} - a)}{b}$$
$$Na_{LF} = \frac{(M0_{LF} - a)}{b} \quad (2)$$

Finally, we calculated the TSC in each ROI as follows:

$$TSC = Na_{SF} + Na_{LF} \quad (3)$$

Each ROI had to be almost totally (>99.9%) included in the brain mask of the individual patient and in the brain masks of at least half of all HC. Finally, to limit the partial volume effect related to CSF, patient ROIs with high CSF contains—estimated with structural image segmentation—relative to HC ($|z\text{-score}_{CSF}| > 1.96$) were also discarded. If after this final step, a patient had no remaining EZ ROIs, the patient was entirely discarded from the analyzes, reducing the number of investigated patients from 19 to 15.

2.4 | SEEG recordings

Recordings were performed using intracerebral multiple contact electrodes (10–18 contacts with length 2 mm, diameter 0.8 mm, and 1.5 mm apart, Alcis). The electrodes were implanted using a stereotactic surgical robot ROSA™. Cranial CT scan was performed to verify the absence of any complication and the spatial accuracy of the implantation. CT/MRI data co-registration and 3D-reconstructions of patients' brains with electrodes were performed using an in-house open-source software (EpiTools; Medina Villalon et al., 2018) to automatically localize the position of each electrode contact and display the results of signal analysis in each patient's anatomy.

Signals were recorded on a 256-channel Natus system, sampled at 512 Hz and saved on a hard disk (16 bits/sample) using no digital filter. Two hardware filters were present in the acquisition procedure: a high-pass filter (cutoff frequency equal to 0.16 Hz at −3 dB), and an anti-aliasing low-pass filter (cutoff frequency equal to 170 Hz at 512 Hz).

2.5 | SEEG-signal analysis

All signal analyzes were performed in a bipolar montage and computed using the open-source AnyWave software (Colombet et al., 2015) available at https://meg.univ-amu.fr/wiki/AnyWave. For each patient, a bipolar montage containing pairs of contiguous contacts, of which at least one is within the gray matter, was generated

automatically using an open-source software GARDEL (Graphical user interface for Automatic Registration and Depth Electrodes Localization; Medina Villalon et al., 2018) available at https://meg.univ-amu.fr/wiki/GARDEL:presentation. In brief, co-registration of post-implantation CT scan with electrodes with pre-implantation MRI scan was performed, followed by an automatic recognition, anatomical localization and labeling of each electrode contact, to obtain patient's specific 3D maps with SEEG electrodes. Each contact was assigned automatically by GARDEL to the cerebral gray (GM) or white matter (WM), or the CSF. At the end, contact coordinates with their respective attributions are saved in the reference frame of T_1-weighted images in the patient's MRI space and are used for SEEG montage generation, visualization of signal processing results at the single contact level and for establishing ROI for multimodal imaging measures (see below). The automatically obtained bipolar SEEG gray matter montage is then visually checked by an expert (JM) and contacts with an artifact SEEG signal is excluded from the final data set.

The epileptogenicity of different brain structures was assessed by quantitative SEEG-signal analysis using the Epileptogenicity Index (EI; Bartolomei et al., 2008). The EI combines analysis of both spectral and temporal features of SEEG signals, respectively, related to the propensity of a brain area to generate fast discharges (12.4–127 Hz), and to how early this area becomes involved in seizure. A normalized EI value is used, ranging from 0 to 1. If there is no involvement of the brain structure, the EI = 0 (no epileptogenicity), whereas if the brain structure generates a rapid discharge and the time to seizure onset is minimal, the EI = 1 (maximal epileptogenicity). In each patient, maximal EI values from at least three representative seizures were computed. We labeled each pair of bipolar SEEG contacts as belonging to the EZ, PZ, or NIZ, as defined by EI, based on previous studies (Aubert et al., 2009; Lagarde et al., 2019). An EI value of 0.4 and higher was set as a threshold to define a structure as belonging to the EZ. The PZ was defined as brain areas with 0.1 < EI <0.4, with sustained discharge during the seizure course. The NIZ was defined as all other brain structures (Figure 1a).

2.6 | ROI definition

For each patient, all bipolar contacts of the SEEG data set used for quantitative signal analysis (after excluding bipolar contacts of which both are within the WM or the CSF or disclosing an artifact SEEG signal) were then used as ROI for multimodal imaging measures. GARDEL software (Medina Villalon et al., 2018) provided the MRI voxel coordinates of electrode contacts allowing the definition of spherical ROIs for sodium and metabolite quantification in the patient's native space. As each bipolar SEEG channel recording corresponds to the signal differential across two adjacent electrode contacts (with 2 mm length and 1.5 mm apart), spherical ROIs of 5 mm radius were positioned with a center between two adjacent electrode contacts (Ridley, Marchi, et al., 2017; Figure 1b). To deal with possible contamination of the brain sodium signal by an over-representation of CSF in patients, we discarded ROIs with overly high $z\text{-score}_{CSF}$ (see Section 2.3). Anatomical references were the MPRAGE volumes for ^{1}H-MRSI (3 T) and the MP2RAGE volumes for ^{23}Na-MRI (7 T). ANTS brain extraction function was applied to all anatomical and ^{23}Na-MRI images. Each subject's (patients and controls) anatomical images were coregistered onto their respective ^{1}H-MRSI and ^{23}Na-MRI maps. Each individual anatomical volume was also spatially normalized onto the MNI 152 template to obtain the direct and reverse spatial transforms for each subject. ROIs were projected from the patient native space to MNI space, and back-projected from MNI to each HC native space (ANTS). This procedure allowed us to extract normative values of ^{23}Na MRI and ^{1}H-MRSI data from the control group for each ROI defined in each patient. Details about the number of ROIs retained after exclusion procedure at each step are summarized in Table S1. Total numbers of ROIs within the regions corresponding to the EZ, PZ and NIZs used for each imaging modality are summarized in Table S2. ^{23}Na-MRI and ^{1}H-MRSI raw value mean ± standard deviation and percentage of variation in EZ, PZ and NIZ compared to controls are summarized in Table S3.

2.7 | Statistical analysis

We performed a group comparison of sodium and metabolites levels across the three ROI classes, EZ, PZ, and NIZ, to decipher subtle and specific homeostatic and metabolic modifications among patients compared to HCs. To account for brain sodium and metabolite variability across participants, sodium and metabolite levels had to be normalized across participants. Thus, each patient's sodium concentrations and metabolites levels in each ROI were expressed as *z*-scores with respect to the same mean quantities from the corresponding ROI in HCs. Normalization of HCs' sodium concentrations and metabolites levels was done using a leave-one-out procedure, *z*-scoring control's quantities relative to the same ROI in other controls' sodium concentrations and metabolites levels.

We compared patients and HCs, looking for different sodium concentration and/or metabolic change profiles between them, and between different region categories (described in Section 2.5). Significant group differences of *z*-scores were analyzed using a bootstrap two-tailed Welch's *t*-test procedure (Efron & Tibshirani, 1993). Achieved significance levels (ASLs) (equivalent to exact *p* values) were obtained after 1 million random samplings, then corrected for multiple comparisons using false discovery rate (FDR; Benjamini & Hochberg, 1995).

To investigate the relationship between sodium concentrations and metabolites levels, we evaluated how well sodium concentration can be predicted from metabolite profiles. Hence, we performed a multiple linear regression analysis (Jobson, 1991) using Statsmodels (Seabold & Perktold, 2010) on all ROIs, with NAA, Cho, and tCr *z*-scores as predictors to compute the linear model for each ^{23}Na-MRI measures (*f* and TSC) *z*-scores.

3 | RESULTS

3.1 | Clinical features

Patients' clinical characteristics are summarized in Table 1. The mean age at epilepsy onset was 13 years (range 0.1–40), mean duration of epilepsy was 18 years (range 4–31). The mean seizure frequency was 26 per month (range 2–120). Anatomical MRI was normal in 15 (71%) and showed a structural abnormality in 4 (29%) cases. Eleven out of 19 patients underwent curative surgical procedure following SEEG exploration. Of the remaining eight, six patients were recused from surgery because of bilaterality of the EZ or of a high risk of post-surgical functional impairment, one became seizure-free after SEEG-guided thermocoagulations and one refused surgery. The post-surgical outcome was favorable in seven (Engel class I (seizure-free) and class II (almost seizure-free), $n = 7$, 64%) and with worthwhile improvement in four cases (Engel class III, 34%). Epilepsy etiology, according to histopathological findings, was: focal cortical dysplasia (FCD) type I (non-detectable on MRI) in five patients, FCD type II in two, FCD type III in one, and slight gliosis in two. One patient underwent laser-guided interstitial thermosurgery for an MRI-diagnosed DNET, with no histology available.

From the initial sample of 19 patients and according to the quality thresholds previously described, data analyzes were conducted in 15 patients for ^{23}Na-MRI and 17 patients for ^{1}H-MRSI and 13 considering patients with both data sets (Table 1). Patients and HCs did not significantly differ in terms of age and sex, neither in the ^{23}Na-MRI associated patient group (Wilcoxon rank sum, $w = -0.36$, $p = .72$; χ^2 (1, $N = 33$) = 0.26, $p = .88$) nor ^{1}H-MRSI associated patient group (Wilcoxon rank sum, $w = 0.58$, $p = .56$; χ^2 (1, $N = 42$) = 0.038, $p = .98$).

3.2 | Ion homeostasis and metabolic profiles in patients

TSC was increased in epileptic patients relative to corresponding ROIs in HCs in all types of electrophysiologically defined regions (i.e., EZ, PZ, and NIZ), with no significant differences between these three region categories within patients (see Table 2 and Figure 3a). The short fraction f was significantly increased in EZ relative to corresponding ROIs in HCs, but was not significantly different compared to HCs in regions corresponding to PZ and NIZ. In patients, f within EZ was also significantly increased relative to PZ and NIZ.

In patients, NAA levels were significantly decreased in all types of regions relative to controls (see Table 2 and Figure 3b). In addition, NAA was significantly decreased in EZ compared to PZ and NIZ. In patients relative to controls, tCho levels were significantly increased in EZ, decreased in NIZ and not significantly different in PZ; tCr levels were not significantly different in EZ and PZ but significantly decreased in NIZ.

3.3 | Association between ionic and metabolic parameters

To study the relationship between sodium concentrations and metabolite levels, a multiple linear regression analysis was conducted. We evaluated the prediction of each ^{23}Na-MRI measure from all ^{1}H-MRSI measures in each region category, namely EZ, PZ, and NIZ, setting Bonferroni corrected p for coefficient t test at .05/2*3*3 = .0028.

Significant regression equations were found for the model predicting TSC from metabolites predictors alone in PZ ($F(3, 80) = 10.76$, $p < .0028$, $R^2 = 0.29$) and in NIZ ($F(3, 283) = 16.25$, $p < .0028$, $R^2 = 0.15$) but not in EZ ($F(3, 34) = 1.29$, $p = .295$, $R^2 = 0.1$). We observed a negative association between TSC and NAA in PZ ($\beta = -0.87$, $p < .0028$) and in NIZ ($\beta = -0.45$, $p < .0028$). We also found a negative association between TSC and Cho and a trend towards a positive association with tCr in NIZ (Table 3). Multiple linear regression analysis of f does not provide significant results in any ROI.

4 | DISCUSSION

This work aimed to explore both in vivo ion homeostasis and metabolic alterations in focal drug-resistant epilepsy investigated by SEEG. We observed global brain impact in patients reflected by consistent multimodal alterations including an increase of TSC as well as decreases in NAA levels within all categories of electrically defined regions, namely EZ, PZ, and NIZ. Interestingly, the EZ showed a characteristic pattern with significantly higher f, as well as significantly lower NAA and higher Cho levels. TSC exhibits strong association with metabolites, especially in the PZ and NIZ. These imaging features likely reflect both hyperexcitability and tissue alterations with a specific pattern of f for the epileptogenic tissues.

4.1 | Deciphering sodium homeostasis processes with 7 T ^{23}Na MRI

Accumulation of TSC is a feature described in a number of neurological diseases including multiple sclerosis (Maarouf et al., 2017; Zaaraoui et al., 2012), amyotrophic lateral sclerosis (Grapperon et al., 2019), Hungtington's disease (Reetz et al., 2012), and epilepsy (Ridley, Marchi, et al., 2017). Attempts to model processes involved in TSC increases have been proposed considering in vitro experiments showing increases of intracellular sodium concentrations in multiple sclerosis (Waxman, 2006). In this model, an increase in TSC – the TSCis usually associated with an elevation of *intracellular* sodium concentration due to an influx of sodium resulting from a dysfunction of the sodium–potassium pump (Na+/K+ pump) (Pike et al., 1985). However, though sensitive, TSC is not specific to altered homeostasis between sodium compartments.

TSC alterations in humans in vivo have largely been demonstrated at 3 T. Here, to improve our understanding of the dysregulation

TABLE 2 Bootstrap ped *t* value followed by *p* (or ASL, the bootstrapped achieved significance level)

	EZ versus HC	PZ versus HC	NIZ versus HC	EZ versus PZ	EZ versus NIZ	PZ versus NIZ
f	2.96, $3.8{\cdot}10^{-3}$		–	2.51, 0.012	2.43, 0.015	–
TSC	3.73, $2.5{\cdot}10^{-4}$	5.35, $1.0{\cdot}10^{-6}$	12.83, $p < 1.0{\cdot}10^{-6}$	–	–	–
NAA	−6.03, $p < 1.0{\cdot}10^{-6}$	−4.51, $8.0{\cdot}10^{-6}$	−9.46, $p < 1.0{\cdot}10^{-6}$	–	−2.32, 0.022	–
Cho	3.31, $1.8{\cdot}10^{-3}$	–	−2.75, $6.4{\cdot}10^{-3}$	–	3.94, $1.3{\cdot}10^{-4}$	2.47, 0.015
tCr	–	–	−7.42, $p < 1.0{\cdot}10^{-6}$	–	–	–

Note: FDR-correction yielded $p < .016$ as threshold for tested ^{23}Na-MRI measurements, and $p < .022$ for tested ^{1}H-MRSI.
Abbreviations: ASL, achieved significance level; EZ, epileptogenic zone; HC, healthy control; NIZ, noninvolved zone; PZ, propagation zone.

mechanisms affecting the sodium ion homeostasis in epilepsy, we used 7 T ^{23}Na MRI. Ultra-high field offers the opportunity to study the complexity of the T_2^* decays of the ^{23}Na MR signal influenced by the quadrupolar relaxation. Indeed, multi-exponential relaxations of this three-half spin reflect the time-dependent relative position of the quadrupolar moments of sodium nuclei and the electric field gradients of charged molecules at their vicinity. The multi-TE density adapted radial ^{23}Na, ultra-short echo time (UTE) approach used here permits the characterization of the signal decay components through a bi-exponential fit. While related, the signal fraction of the short T_2^* decay component (*f*), and the TSC may reflect different consequences of ion homeostasis dysregulation (Ridley et al., 2018).

Normal physiological neuronal activity has been observed to dynamically alter sodium signal across different TEs, in a manner consilient with fMRI and consistent with physiological mechanisms that should dominate at different points of "activation" (Bydder et al., 2019). Using dynamic sodium MRI acquisition compared to BOLD functional MRI, variations in sodium signals recorded at different TEs (0.2 ms, 10 ms, and 19 ms) during a right finger tapping task showed a slightly increased TSC (TE = 0.2 ms) in the activated left contralateral motor area interpreted as increased cerebral blood volume, and a more drastic signal decrease at longer TEs considered, at least in part, to a decrease in extracellular contributions due a reduced extracellular volume (ECV) fraction (Antonio et al., 2016; Dietzel et al., 1982; Lux et al., 1986), while reverse signal variations were observed in the deactivated motor area ipsilateral to movement. The *f* metric, reflecting the variations in the ratio of apparent short and long T_2^* sodium signal decays, enables to pool in a single parameter these effects seen at different TEs, and has the potential to locate regions with abnormal excitability as shown in the present study.

4.2 | Sodium changes in epilepsy

In the context of epilepsy, abnormal TSC increase has been found in EZ and to a lesser extent also in other regions of the brain at 3 T (Ridley, Marchi, et al., 2017). In addition, rat models of acquired epilepsy have reported persistent TSC increases in affected cortices in response to kainate-induced epileptogenesis (Mori et al., 2000; Wang et al., 1996). TSC may incorporate various processes including both structural reorganization and dysregulation of ionic homeostasis. Indeed, several structural modifications can impact ^{23}Na-MRI signals, particularly changes in the ECV. Cell shrinkage and cerebral atrophy could lead to ECV increase, and subsequently to increases in TSC. Both have been reported in epilepsy, localized in the epileptic areas, but also often extended to the nonepileptogenic regions (Bernhardt et al., 2009; Dingledine et al., 2014; Liu et al., 2005; Voets et al., 2017). Thus, even though excessively high CSF levels ($z\text{-score}_{CSF} > 1.95$) led to the removal of a ROI from consideration, its contribution cannot be entirely ruled out. In addition, ECV increase was recently shown to be related to neuronal excitability (Colbourn et al., 2019). Moreover, increases of perivascular space were also reported in epilepsy (Feldman et al., 2018, 2019), and could contribute to TSC accumulation due to the CSF surrounding the vessels. Recently, venous blood was also demonstrated to have an impact on total sodium signal (Driver et al., 2020), leading to overestimation of sodium concentration measures in case of atrophy. In addition, reactive astrogliosis and microgliosis (Devinsky et al., 2013; Seifert & Steinhäuser, 2013; Sofroniew & Vinters, 2010) can be associated with epilepsy implying changes of astrocytes proportion, size (Boscia et al., 2016), and ion homeostasis, leading to surrounding cell homeostasis disruption (Karus et al., 2015). Interestingly, TSC was also shown to correlate with conductivity at 3 T (Liao et al., 2019).

Beyond general explanations for alterations of TSC in epilepsy, cortices subject to different epileptiform manifestations (EZ, PZ, and NIZ) are likely to differ in underlying pathological mechanisms, something that was probed in the current work through the use of a multiparametric approach. While keeping in mind that both sodium signal fractions (i.e., short and long) will contain contributions from extracellular sodium—albeit with potentially different weightings—a plausible reason for the concomitant EZ-specific increase relative to both HC and other cortices of both *f* and TSC is an increase of intracellular sodium concentration. This would be consistent with a range of known mechanisms associated with the EZ, while TSC increase outside the EZ in the absence of changes in *f* may be related to structural changes combined with preserved perfusion, which is usually decreased in the EZ during the interictal period (Kojan et al., 2021; Wang et al., 2018).

Sodium homeostasis dysregulation in the EZ could be induced by several mechanisms affecting ion channels such as (i) alterations in type II and III voltage-gated sodium channel (VGNC) properties (Bartolomei et al., 1997; Gastaldi et al., 1997; Gorter et al., 2010;

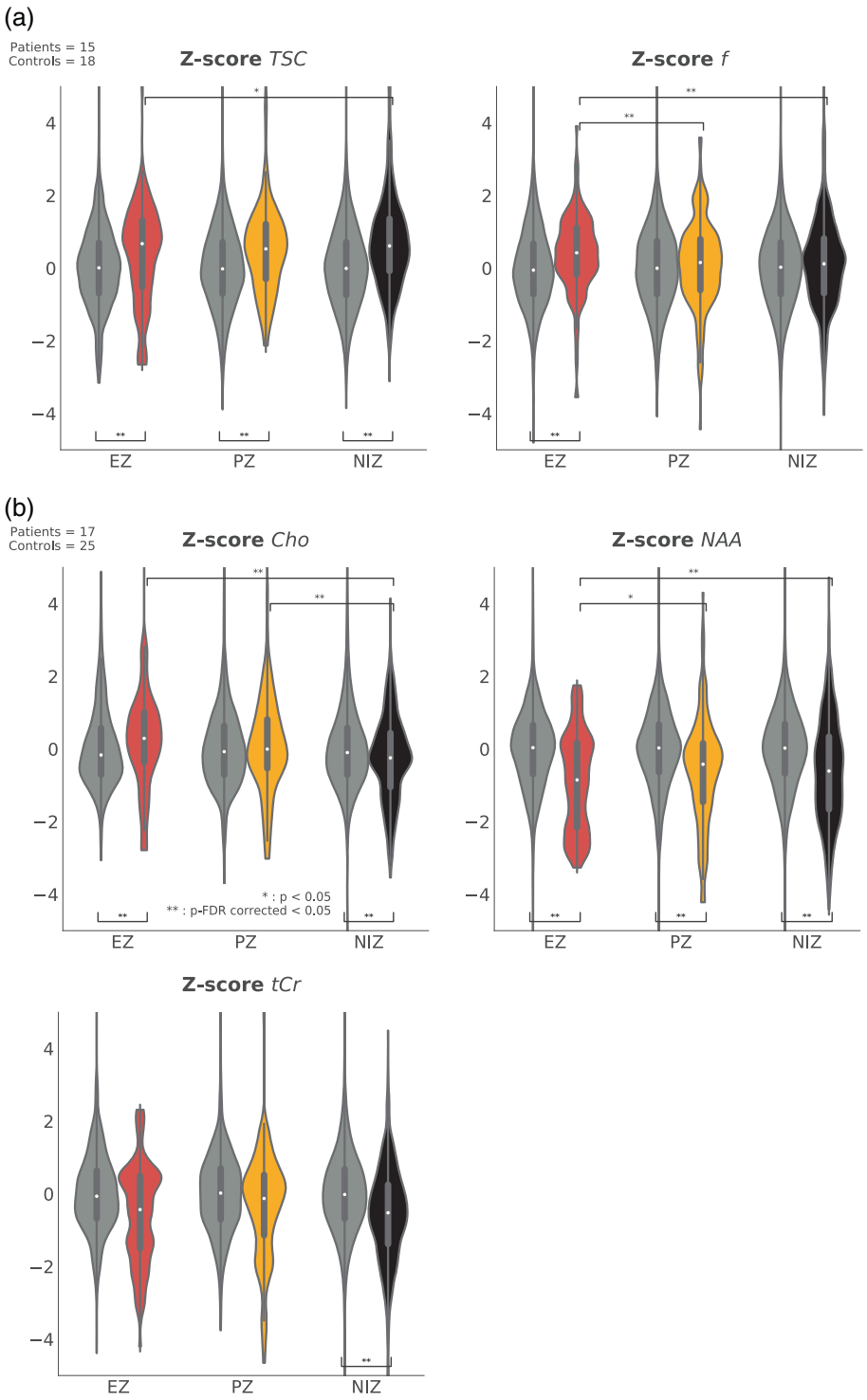

FIGURE 3 Violin plot of mean *z*-scores of sodium (a) and metabolite estimates (b) observed in patients within epileptogenic zones (EZs; red), propagation zones (PZs; yellow), and non-involved zones (NIZs; black), compared to healthy controls (HCs; gray). Asterisks indicate significant differences between patients and controls when under violins, and between regions within patients when above violins. *: *p*-uncorrected < .05. **: *p*-FDR < .05.

Lombardo et al., 1996), (ii) incomplete inactivation of sodium channels and a consequent increase in persistent sodium currents (Mantegazza et al., 2010; Oliva et al., 2012), and (iii) the reduced efficiency of clearance by the Na+/K+ pump induced by a lack in ATP supplies (Folbergrová & Kunz, 2012; Grisar et al., 1992; Kovac et al., 2017).

Other mechanisms secondary to hyperexcitability or energy failure affecting astrocytes could also lead to an alteration of sodium homeostasis and an increase in intracellular sodium (Gerkau et al., 2017; Kirischuk et al., 2012; Rose & Karus, 2013). Indeed, as a consequence of hyperexcitability, astrocytes may uptake sodium through various transporters (sodium-potassium-chloride co-transporter (NKCC1), sodium-bicarbonate co-transporter (NBC), sodium-proton exchanger (NHE), and sodium-calcium exchanger (NCX)) increasing their intracellular sodium concentrations. Heightened intracellular sodium concentrations reduce the electrochemical gradient for glutamate uptake (Karus et al., 2015) by the excitatory

TABLE 3 Summary of multiple linear regression analysis for TSC and *f*

		Parameters	Coefficients	*p*		
TSC	EZ	Const	0.43	0.191	Df residuals	34
		Cho	−0.05	0.837	Df Model	3
		NAA	−0.59	0.0743	R^2	0.1
		tCr	0.39	0.229	*F* (*p*)	1.29 (0.295)
	PZ	Const	0.86	$8.89{\cdot}10^{-5}$	Df residuals	80
		Cho	−0.33	0.0787	Df Model	3
		NAA	−0.87	$9.02{\cdot}10^{-4}$*	R^2	0.29
		tCr	0.56	0.0408	*F* (*p*)	10.76 ($5.13{\cdot}10^{-6}$)
	NIZ	Const	0.94	$1.60{\cdot}10^{-17}$	Df residuals	283
		Cho	−0.29	$6.53{\cdot}10^{-3}$*	Df Model	3
		NAA	−0.45	$1.90{\cdot}10^{-6}$*	R^2	0.15
		tCr	0.25	0.0392	*F* (*p*)	16.25 ($8.96{\cdot}10^{-10}$)
f	EZ	Const	0.51	$6.15{\cdot}10^{-3}$	Df residuals	34
		Cho	−0.33	0.0114	Df Model	3
		NAA	0.01	0.967	R^2	0.18
		tCr	0.24	0.17	*F* (*p*)	2.48 (0.0781)
	PZ	Const	−0.12	0.448	Df residuals	80
		Cho	0.03	0.832	Df Model	3
		NAA	−0.28	0.154	R^2	0.03
		tCr	0.12	0.572	*F* (*p*)	0.94 (0.425)
	NIZ	Const	0.02	0.791	Df residuals	283
		Cho	0.11	0.158	Df Model	3
		NAA	0.04	0.587	R^2	0.01
		tCr	−0.16	0.0615	*F* (*p*)	1.4 (0.244)

Note: Bonferroni corrected *p* values are highlighted in bold followed by an asterisk, while uncorrected *p* values are in bold without asterisk.
Abbreviations: Cho, choline compound; EZ, epileptogenic zone; HC, healthy control; NAA, N-acetyl aspartate; NIZ, noninvolved zone; PZ, propagation zone; tCr, total creatine; TSC, total sodium concentration.

amino acid transporter (EAAT), a transmembrane transporter of sodium and glutamate from peri-synaptic extracellular space into astrocytes, ensuring ion and neurotransmitter clearance. Then extracellular glutamate concentration increases and eventually downregulates EAAT (Rose & Karus, 2013); as astrocytes store energy supplies, astrocytic energy failure is critical for ion homeostasis of both astrocytes and the surrounding neurons. The reduced availability of ATP associated with increases in intracellular sodium also leads to the dysregulation of homeostasis for other ions such as potassium, calcium and proton, resulting in excitotoxicity (Gerkau et al., 2017). During hyperexcitability, intracellular pH decreases which leads to sodium uptake via NBC, VGNC, or Na+/K+ pump, among others. This reduced intracellular pH was suggested to result from lack of NHE1 (Zhao et al., 2016). The relationship between reduced intracellular pH and increased intracellular sodium was also shown in epilepsy during hepatic encephalitis (Kelly et al., 2009) with ammonium intoxication. The intoxication of cerebral tissue promotes intracellular pH increase (in particular in astrocytes) resulting in intracellular sodium increase.

4.3 | Metabolic changes

The multimodal nature of our investigation provides further evidence of an alteration in ionic homeostasis in epilepsy due to a disruption of metabolic energy supply. The decreased NAA we observed has been consistently associated with neuronal death, mitochondrial dysfunction (Stefano et al., 1995), and subsequent ATP decrease (Vagnozzi et al., 2007). NAA decrease in the EZ has been widely reported since the 90s (Guye et al., 2005; Hugg et al., 1993; Kuzniecky et al., 1998; Petroff et al., 2003; Simister et al., 2002; van der Hel et al., 2013). While more recent research indicates that decreases in NAA extend to other regions, those involved in seizures remain the most affected (Guye et al., 2005; Lundbom et al., 2001; Mueller et al., 2011) as is the case for TSC in this study. This finding is in line with our energetic failure hypothesis; however, it should be noted that we were unable to observe a significant association between these two measures in EZ when explored by multiple linear regression.

Increased Cho has also been reported in temporal lobe epilepsy (Achten et al., 1997; Simister et al., 2009) and is frequently associated

with cellular proliferation and increased membrane turnover (Miller, 1991; Urenjak et al., 1993). These processes are likely to be linked to structural changes associated with epileptogenic lesions such as tumors, tumor-like tissue, and gliosis (van der Hel et al., 2013). The Cho decrease in NIZ was unexpected and has not been previously reported to our knowledge. It could result from reduced cellular density or neuronal loss extending beyond the EZ.

In our cohort, tCr was significantly decreased in NIZ only. Heighted tCr was previously related to decreased intracellular energy status or reactive astrocytes in the literature (Achten, 1998; Urenjak et al., 1993). This result also points to alterations beyond EZ potentially accompanying structural changes and cognitive comorbidities (Kreis et al., 1992; Kreis & Ross, 1992).

Interestingly, sodium and metabolite levels did not reveal significant relations in EZ. This could be linked to the disruption of the homeostasis between ionic and metabolic processes due to the pathology of the epileptogenic tissue. This failure of homeostatic regulation could therefore be a feature of the EZ to be potentially used for its definition. This is in line with the decorrelation between BOLD and SEEG signals, for instance, we found in the EZ when measuring functional connectivity in a previous study (Ridley, Wirsich, et al., 2017). However, this lack of relations between sodium and metabolites in the EZ could also be due to the epileptogenic lesions that could affect sodium and metabolite contents differently.

4.4 | Technical limitations

For both ^{23}Na-MRI and ^{1}H-MRSI, CSF signal contribution is critical as it can clearly bias the data. MIDAS software handled this bias for ^{1}H-MRSI data (Lecocq et al., 2015). For ^{23}Na-MRI we corrected for partial volume effect and removed ROIs with remaining CSF after segmentation. We designed a quality check procedure inspired by (Ridley, Marchi, et al., 2017) in order to get rid of this CSF contribution. Despite this, it is impossible to totally delimit the partial volume effect completely for the moment, neither for ^{1}H-MRSI nor ^{23}Na-MRI. Another limitation is inherent to the SEEG procedure, which suffers from limited spatial sampling, whereas MRI gives access to information across the entire brain. Conversely, the pathological specificity offered by SEEG is considered gold-standard and beyond what is possible with anatomically defined and atlas-derived ROIs.

4.5 | Conclusion and perspectives

An increase of the signal fraction of the short T_2^* decay component (f) was found to be associated with the EZ, whereas increased TSC was not limited to epileptogenic regions. Taken together with the patterns of metabolite changes our results are in line with the energetic failure hypothesis in epileptic regions associated with widespread tissue changes beyond electrically abnormal areas. Here, a multimodal approach has allowed parallel insights supporting pathological processes in epilepsy. This and additional combinations—including, for example, ^{31}P-MRSI, which provides information about energy metabolism via ATP quantification and pH estimation—could further strengthen the delineation of the EZ as this *non-invasive* information would complement the current presurgical evaluation in patients suffering from drug-resistant focal epilepsy.

AUTHOR CONTRIBUTIONS

Mikhael Azilinon: Investigation; methodology; data curation; formal analysis; writing – original draft. **Julia Makhalova**: Resources; data curation; formal analysis; writing – review and editing. **Wafaa Zaaraoui**: Funding acquisition; writing – review and editing. **Samuel Medina Villalon**: Methodology. **Patrick Viout**: Formal analysis. **Tangi Roussel**: Methodology; writing – review and editing. **Mohamed M. El Mendili**: Methodology; writing – review and editing. **Jean-Philippe Ranjeva**: Supervision; validation; methodology; writing – original draft. **Fabrice Bartolomei**: Funding acquisition; resources; writing – review and editing. **Viktor Jirsa**: Funding acquisition; supervision, writing – review and editing. **Maxime Guye**: Project administration; funding acquisition; resources; conceptualization; supervision; validation; writing – original draft.

ACKNOWLEDGMENTS

The authors would like to thank L. Pini, C. Costes, and V. Gimenez for data acquisition and study logistics. The authors would also like to thank A. Ivanov and C. Bernard for helpful discussions. This study has received support from the French government under the "Programme Investissements d'Avenir," Excellence Initiative of Aix–Marseille University – A*MIDEX (AMX-19-IET-004), 7TEAMS Chair, EPINOV (Grant ANR-17-RHUS-0004) and ANR (ANR-17-EURE-0029); and from the European Union's Horizon 2020 Framework Program for Research and Innovation under the Specific Grant agreement nos. 785907 (Human Brain Project SGA2) and 945539 (Human Brain Project SGA3).

CONFLICTS OF INTEREST

The authors declare no conflicts of interest.

DATA AVAILABILITY STATEMENT

The data that support the findings of this study are available on request from the corresponding author. The data are not publicly available due to sensitive information that could compromise the privacy of research participants.

ORCID

Mikhael Azilinon https://orcid.org/0000-0001-8094-2249
Jean-Philippe Ranjeva https://orcid.org/0000-0001-8073-102X

REFERENCES

Achten, E. (1998). Aspects of proton MR spectroscopy in the seizure patient. *Neuroimaging Clinics of North America*, *8*(4), 849–862.

Achten, E., Boon, P., Kerckhove, T. V. D., Caemaert, J., Reuck, J. D., & Kunnen, M. (1997). Value of single-voxel proton mr spectroscopy in

temporal lobe epilepsy. *American Journal of Neuroradiology*, *18*(6), 1131–1139.

Aja-Fernandez, S., Alberola-Lopez, C., & Westin, C. (2008). Noise and signal estimation in magnitude MRI and Rician distributed images: A LMMSE approach. *IEEE Transactions on Image Processing*, *17*(8), 1383–1398. https://doi.org/10.1109/TIP.2008.925382

Antonio, L. L., Anderson, M. L., Angamo, E. A., Gabriel, S., Klaft, Z.-J., Liotta, A., Salar, S., Sandow, N., & Heinemann, U. (2016). In vitro seizure like events and changes in ionic concentration. *Journal of Neuroscience Methods*, *260*, 33–44. https://doi.org/10.1016/j.jneumeth.2015.08.014

Aubert, S., Wendling, F., Regis, J., McGonigal, A., Figarella-Branger, D., Peragut, J.-C., Girard, N., Chauvel, P., & Bartolomei, F. (2009). Local and remote epileptogenicity in focal cortical dysplasias and neurodevelopmental tumours. *Brain*, *132*(11), 3072–3086. https://doi.org/10.1093/brain/awp242

Avants, B. B., Tustison, N. J., Song, G., Cook, P. A., Klein, A., & Gee, J. C. (2011). A reproducible evaluation of ANTs similarity metric performance in brain image registration. *NeuroImage*, *54*(3), 2033–2044. https://doi.org/10.1016/j.neuroimage.2010.09.025

Bartolomei, F., Chauvel, P., & Wendling, F. (2008). Epileptogenicity of brain structures in human temporal lobe epilepsy: A quantified study from intracerebral EEG. *Brain*, *131*(7), 1818–1830. https://doi.org/10.1093/brain/awn111

Bartolomei, F., Gastaldi, M., Massacrier, A., Planells, R., Nicolas, S., & Cau, P. (1997). Changes in the mRNAs encoding subtypes I, II and III sodium channel alpha subunits following kainate-induced seizures in rat brain. *Journal of Neurocytology*, *26*(10), 667–678. https://doi.org/10.1023/a:1018549928277

Benjamini, Y., & Hochberg, Y. (1995). Controlling the false discovery rate: A practical and powerful approach to multiple testing. *Journal of the Royal Statistical Society. Series B (Methodological)*, *57*(1), 289–300.

Bernhardt, B. C., Rozen, D. A., Worsley, K. J., Evans, A. C., Bernasconi, N., & Bernasconi, A. (2009). Thalamo–cortical network pathology in idiopathic generalized epilepsy: Insights from MRI-based morphometric correlation analysis. *NeuroImage*, *46*(2), 373–381. https://doi.org/10.1016/j.neuroimage.2009.01.055

Boscia, F., Begum, G., Pignataro, G., Sirabella, R., Cuomo, O., Casamassa, A., Sun, D., & Annunziato, L. (2016). Glial Na^+-dependent ion transporters in pathophysiological conditions: Glial Na^+-dependent transporters in CNS diseases. *Glia*, *64*(10), 1677–1697. https://doi.org/10.1002/glia.23030

Burstein, D., & Springer, C. S. (2019). Sodium MRI revisited. *Magnetic Resonance in Medicine*, *82*(2), 521–524. https://doi.org/10.1002/mrm.27738

Bydder, M., Zaaraoui, W., Ridley, B., Soubrier, M., Bertinetti, M., Confort-Gouny, S., Schad, L., Guye, M., & Ranjeva, J.-P. (2019). Dynamic 23Na MRI-A non-invasive window on neuroglial-vascular mechanisms underlying brain function. *NeuroImage*, *184*, 771–780. https://doi.org/10.1016/j.neuroimage.2018.09.071

Colbourn, R., Naik, A., & Hrabetova, S. (2019). ECS dynamism and its influence on neuronal excitability and seizures. *Neurochemical Research*, *44*(5), 1020–1036. https://doi.org/10.1007/s11064-019-02773-w

Colombet, B., Woodman, M., Badier, J. M., & Bénar, C. G. (2015). AnyWave: A cross-platform and modular software for visualizing and processing electrophysiological signals. *Journal of Neuroscience Methods*, *242*, 118–126. https://doi.org/10.1016/j.jneumeth.2015.01.017

Devinsky, O., Vezzani, A., Najjar, S., De Lanerolle, N. C., & Rogawski, M. A. (2013). Glia and epilepsy: Excitability and inflammation. *Trends in Neurosciences*, *36*(3), 174–184. https://doi.org/10.1016/j.tins.2012.11.008

Dietzel, I., Heinemann, U., Hofmeier, G., & Lux, H. D. (1982). Stimulus-induced changes in extracellular Na+ and Cl- concentration in relation to changes in the size of the extracellular space. *Experimental Brain Research*, *46*(1), 73–84. https://doi.org/10.1007/BF00238100

Dingledine, R., Varvel, N. H., & Dudek, F. E. (2014). When and how do seizures kill neurons, and is cell death relevant to epileptogenesis? In H. E. Scharfman & P. S. Buckmaster (Eds.), *Issues in clinical epileptology: A view from the bench* (Vol. 813, pp. 109–122). Springer. https://doi.org/10.1007/978-94-017-8914-1_9

Donadieu, M., Le Fur, Y., Maarouf, A., Gherib, S., Ridley, B., Pini, L., Rapacchi, S., Confort-Gouny, S., Guye, M., Schad, L. R., Maudsley, A. A., Pelletier, J., Audoin, B., Zaaraoui, W., & Ranjeva, J.-P. (2019). Metabolic counterparts of sodium accumulation in multiple sclerosis: A whole brain 23Na-MRI and fast 1H-MRSI study. *Multiple Sclerosis Journal*, *25*(1), 39–47. https://doi.org/10.1177/1352458517736146

Driver, I. D., Stobbe, R. W., Wise, R. G., & Beaulieu, C. (2020). Venous contribution to sodium MRI in the human brain. *Magnetic Resonance in Medicine*, *83*(4), 1331–1338. https://doi.org/10.1002/mrm.27996

Efron, B., & Tibshirani, R. J. (1993). *An introduction to the bootstrap*. Springer US. https://doi.org/10.1007/978-1-4899-4541-9

Feldman, R. E., Delman, B. N., Pawha, P. S., Dyvorne, H., Rutland, J. W., Yoo, J., Fields, M. C., Marcuse, L. V., & Balchandani, P. (2019). 7T MRI in epilepsy patients with previously normal clinical MRI exams compared against healthy controls. *PLoS One*, *14*(3), e0213642. https://doi.org/10.1371/journal.pone.0213642

Feldman, R. E., Rutland, J. W., Fields, M. C., Marcuse, L. V., Pawha, P. S., Delman, B. N., & Balchandani, P. (2018). Quantification of perivascular spaces at 7 T: A potential MRI biomarker for epilepsy. *Seizure*, *54*, 11–18. https://doi.org/10.1016/j.seizure.2017.11.004

Folbergrová, J., & Kunz, W. S. (2012). Mitochondrial dysfunction in epilepsy. *Mitochondrion*, *12*(1), 35–40. https://doi.org/10.1016/j.mito.2011.04.004

Gastaldi, M., Bartolomei, F., Massacrier, A., Planells, R., Robaglia-Schlupp, A., & Cau, P. (1997). Increase in mRNAs encoding neonatal II and III sodium channel a-isoforms during kainate-induced seizures in adult rat hippocampus. *Brain Research. Molecular Brain Research*, *44*, 179–190.

Gerkau, N. J., Rakers, C., Petzold, G. C., & Rose, C. R. (2017). Differential effects of energy deprivation on intracellular sodium homeostasis in neurons and astrocytes: Effects of energy deprivation on cellular sodium. *Journal of Neuroscience Research*, *95*(11), 2275–2285. https://doi.org/10.1002/jnr.23995

Gorter, J. A., Zurolo, E., Iyer, A., Fluiter, K., Van Vliet, E. A., Baayen, J. C., & Aronica, E. (2010). Induction of sodium channel Nax (SCN7A) expression in rat and human hippocampus in temporal lobe epilepsy: SCN7A expression in TLE. *Epilepsia*, *51*(9), 1791–1800. https://doi.org/10.1111/j.1528-1167.2010.02678.x

Grapperon, A.-M., Ridley, B., Verschueren, A., Maarouf, A., Confort-Gouny, S., Fortanier, E., Schad, L., Guye, M., Ranjeva, J.-P., Attarian, S., & Zaaraoui, W. (2019). Quantitative brain sodium MRI depicts corticospinal impairment in amyotrophic lateral sclerosis. *Radiology*, *292*(2), 422–428. https://doi.org/10.1148/radiol.2019182276

Grimaldi, S., El Mendili, M. M., Zaaraoui, W., Ranjeva, J.-P., Azulay, J.-P., Eusebio, A., & Guye, M. (2021). Increased sodium concentration in substantia Nigra in early Parkinson's disease: A preliminary study with ultra-high field (7T) MRI. *Frontiers in Neurology*, *12*, 1610. https://doi.org/10.3389/fneur.2021.715618

Grisar, T., Guillaume, D., & Delgado-Escuet, A. V. (1992). Contribution of Na+, K+-ATPase to focal epilepsy: A brief review. *Epilepsy Research*, *12*(2), 141–149. https://doi.org/10.1016/0920-1211(92)90034-Q

Guye, M., Le Fur, Y., Confort-Gouny, S., Ranjeva, J.-P., Bartolomei, F., Régis, J., Raybaud, C. A., Chauvel, P., & Cozzone, P. J. (2002). Metabolic and electrophysiological alterations in subtypes of temporal lobe epilepsy: A combined proton magnetic resonance spectroscopic imaging and depth electrodes study. *Epilepsia*, *43*(10), 1197–1209. https://doi.org/10.1046/j.1528-1157.2002.05102.x

Guye, M., Ranjeva, J. P., Le Fur, Y., Bartolomei, F., Confort-Gouny, S., Regis, J., Chauvel, P., & Cozzone, P. J. (2005). 1H-MRS imaging in

intractable frontal lobe epilepsies characterized by depth electrode recording. *NeuroImage*, *26*(4), 1174–1183. https://doi.org/10.1016/j.neuroimage.2005.03.023

Hugg, J. W., Laxer, K. D., Matson, G. B., Maudsley, A. A., & Weiner, M. W. (1993). Neuron loss localizes human temporal lobe epilepsy by in vivo proton magnetic resonance spectroscopic imaging. *Annals of Neurology*, *34*(6), 788–794. https://doi.org/10.1002/ana.410340606

Isnard, J., Taussig, D., Bartolomei, F., Bourdillon, P., Catenoix, H., Chassoux, F., Chipaux, M., Clémenceau, S., Colnat-Coulbois, S., Denuelle, M., Derrey, S., Devaux, B., Dorfmüller, G., Gilard, V., Guenot, M., Job-Chapron, A.-S., Landré, E., Lebas, A., Maillard, L., … Sauleau, P. (2018). French guidelines on stereoelectroencephalography (SEEG). *Neurophysiologie Clinique*, *48*(1), 5–13. https://doi.org/10.1016/j.neucli.2017.11.005

Jobson, J. D. (1991). Multiple linear regression. In J. D. Jobson (Ed.), *Applied multivariate data analysis: Regression and experimental design* (pp. 219–398). Springer. https://doi.org/10.1007/978-1-4612-0955-3_4

Karus, C., Mondragão, M. A., Ziemens, D., & Rose, C. R. (2015). Astrocytes restrict discharge duration and neuronal sodium loads during recurrent network activity: Astrocytes restrict neuronal sodium loads. *Glia*, *63*(6), 936–957. https://doi.org/10.1002/glia.22793

Kelly, T., Kafitz, K. W., Roderigo, C., & Rose, C. R. (2009). Ammonium-evoked alterations in intracellular sodium and pH reduce glial glutamate transport activity. *Glia*, *57*(9), 921–934. https://doi.org/10.1002/glia.20817

Kirischuk, S., Parpura, V., & Verkhratsky, A. (2012). Sodium dynamics: Another key to astroglial excitability? *Trends in Neurosciences*, *35*(8), 497–506. https://doi.org/10.1016/j.tins.2012.04.003

Kojan, M., Gajdoš, M., Říha, P., Doležalová, I., Řehák, Z., & Rektor, I. (2021). Arterial spin labeling is a useful MRI method for Presurgical evaluation in MRI-negative focal epilepsy. *Brain Topography*, *34*(4), 504–510. https://doi.org/10.1007/s10548-021-00833-5

Kovac, S., Dinkova Kostova, A., Herrmann, A., Melzer, N., Meuth, S., & Gorji, A. (2017). Metabolic and homeostatic changes in seizures and acquired epilepsy—Mitochondria, calcium dynamics and reactive oxygen species. *International Journal of Molecular Sciences*, *18*(9), 1935. https://doi.org/10.3390/ijms18091935

Kreis, R., Ernst, T., & Ross, B. D. (1993). Development of the human brain: In vivo quantification of metabolite and water content with proton magnetic resonance spectroscopy. *Magnetic Resonance in Medicine*, *30*(4), 424–437. https://doi.org/10.1002/mrm.1910300405

Kreis, R., & Ross, B. D. (1992). Cerebral metabolic disturbances in patients with subacute and chronic diabetes mellitus: Detection with proton MR spectroscopy. *Radiology*, *184*(1), 123–130. https://doi.org/10.1148/radiology.184.1.1319074

Kreis, R., Ross, B. D., Farrow, N. A., & Ackerman, Z. (1992). Metabolic disorders of the brain in chronic hepatic encephalopathy detected with H-1 MR spectroscopy. *Radiology*, *182*, 19–27. https://doi.org/10.1148/radiology.182.1.1345760

Kuzniecky, R., Hugg, J. W., Hetherington, H., Butterworth, E., Bilir, E., Faught, E., & Gilliam, F. (1998). Relative utility of 1H spectroscopic imaging and hippocampal volumetry in the lateralization of mesial temporal lobe epilepsy. *Neurology*, *51*(1), 66–71. https://doi.org/10.1212/WNL.51.1.66

Lagarde, S., Scholly, J., Popa, I., Valenti-Hirsch, M. P., Trebuchon, A., McGonigal, A., Milh, M., Staack, A. M., Lannes, B., Lhermitte, B., Proust, F., Benmekhbi, M., Scavarda, D., Carron, R., Figarella-Branger, D., Hirsch, E., & Bartolomei, F. (2019). Can histologically normal epileptogenic zone share common electrophysiological phenotypes with focal cortical dysplasia? SEEG-based study in MRI-negative epileptic patients. *Journal of Neurology*, *266*(8), 1907–1918. https://doi.org/10.1007/s00415-019-09339-4

Larivière, S., Bernasconi, A., Bernasconi, N., & Bernhardt, B. C. (2021). Connectome biomarkers of drug-resistant epilepsy. *Epilepsia*, *62*(1), 6–24. https://doi.org/10.1111/epi.16753

Lecocq, A., Le Fur, Y., Maudsley, A. A., Le Troter, A., Sheriff, S., Sabati, M., Donnadieu, M., Confort-Gouny, S., Cozzone, P. J., Guye, M., & Ranjeva, J.-P. (2015). Whole-brain quantitative mapping of metabolites using short echo three-dimensional proton MRSI: 3D-^{1}H-MRSI covering the whole brain. *Journal of Magnetic Resonance Imaging*, *42*(2), 280–289. https://doi.org/10.1002/jmri.24809

Liao, Y., Lechea, N., Magill, A. W., Worthoff, W. A., Gras, V., & Shah, N. J. (2019). Correlation of quantitative conductivity mapping and total tissue sodium concentration at 3T/4T. *Magnetic Resonance in Medicine*, *82*(4), 1518–1526. https://doi.org/10.1002/mrm.27787

Liu, R. S. N., Lemieux, L., Bell, G. S., Sisodiya, S. M., Bartlett, P. A., Shorvon, S. D., Sander, J. W. A. S., & Duncan, J. S. (2005). Cerebral damage in epilepsy: A population-based longitudinal quantitative MRI study. *Epilepsia*, *46*(9), 1482–1494. https://doi.org/10.1111/j.1528-1167.2005.51603.x

Lombardo, A. J., Kuzniecky, R., Powers, R. E., & Brown, G. B. (1996). Altered brain sodium channel transcript levels in human epilepsy. *Molecular Brain Research*, *35*(1–2), 84–90. https://doi.org/10.1016/0169-328X(95)00194-W

Lundbom, N., Gaily, E., Vuori, K., Paetau, R., Liukkonen, E., Rajapakse, J. C., Valanne, L., Häkkinen, A., & Granström, M. (2001). Proton spectroscopic imaging shows abnormalities in glial and neuronal cell pools in frontal lobe epilepsy. *Epilepsia*, *42*(12), 1507–1514. https://doi.org/10.1046/j.1528-1157.2001.15301.x

Lux, H. D., Heinemann, U., & Dietzel, I. (1986). Ionic changes and alterations in the size of the extracellular space during epileptic activity. *Advances in Neurology*, *44*, 619–639.

Maarouf, A., Audoin, B., Pariollaud, F., Gherib, S., Rico, A., Soulier, E., Confort-Gouny, S., Guye, M., Schad, L., Pelletier, J., Ranjeva, J.-P., & Zaaraoui, W. (2017). Increased total sodium concentration in gray matter better explains cognition than atrophy in MS. *Neurology*, *88*(3), 289–295. https://doi.org/10.1212/WNL.0000000000003511

Madelin, G., Lee, J.-S., Regatte, R. R., & Jerschow, A. (2014). Sodium MRI: Methods and applications. *Progress in Nuclear Magnetic Resonance Spectroscopy*, *79*, 14–47. https://doi.org/10.1016/j.pnmrs.2014.02.001

Mantegazza, M., Curia, G., Biagini, G., Ragsdale, D. S., & Avoli, M. (2010). Voltage-gated sodium channels as therapeutic targets in epilepsy and other neurological disorders. *The Lancet Neurology*, *9*(4), 413–424. https://doi.org/10.1016/S1474-4422(10)70059-4

Maudsley, A. A., Darkazanli, A., Alger, J. R., Hall, L. O., Schuff, N., Studholme, C., Yu, Y., Ebel, A., Frew, A., Goldgof, D., Gu, Y., Pagare, R., Rousseau, F., Sivasankaran, K., Soher, B. J., Weber, P., Young, K., & Zhu, X. (2006). Comprehensive processing, display and analysis for in vivo MR spectroscopic imaging. *NMR in Biomedicine*, *19*(4), 492–503. https://doi.org/10.1002/nbm.1025

Medina Villalon, S., Paz, R., Roehri, N., Lagarde, S., Pizzo, F., Colombet, B., Bartolomei, F., Carron, R., & Bénar, C.-G. (2018). EpiTools, a software suite for presurgical brain mapping in epilepsy: Intracerebral EEG. *Journal of Neuroscience Methods*, *303*, 7–15. https://doi.org/10.1016/j.jneumeth.2018.03.018

Miller, B. L. (1991). A review of chemical issues in1H NMR spectroscopy: N-acetyl-l-aspartate, creatine and choline. *NMR in Biomedicine*, *4*(2), 47–52. https://doi.org/10.1002/nbm.1940040203

Moffett, J. R., Arun, P., Ariyannur, P. S., & Namboodiri, A. M. A. (2013). N-Acetylaspartate reductions in brain injury: Impact on post-injury neuroenergetics, lipid synthesis, and protein acetylation. *Frontiers in Neuroenergetics*, *5*, 11. https://doi.org/10.3389/fnene.2013.00011

Mori, Y., Kondziolka, D., Balzer, J., Fellows, W., Flickinger, J. C., Lunsford, L. D., & Thulborn, K. R. (2000). Effects of stereotactic

radiosurgery on an animal model of hippocampal epilepsy. *Neurosurgery*, *46*(1), 157–165; discussion 165-168.

Mueller, S. G., Ebel, A., Barakos, J., Scanlon, C., Cheong, I., Finlay, D., Garcia, P., Weiner, M. W., & Laxer, K. D. (2011). Widespread extrahippocampal NAA/(Cr+Cho) abnormalities in TLE with and without mesial temporal sclerosis. *Journal of Neurology*, *258*(4), 603–612. https://doi.org/10.1007/s00415-010-5799-6

Oliva, M., Berkovic, S. F., & Petrou, S. (2012). Sodium channels and the neurobiology of epilepsy. *Epilepsia*, *53*(11), 1849–1859. https://doi.org/10.1111/j.1528-1167.2012.03631.x

Paling, D., Golay, X., Wheeler-Kingshott, C., Kapoor, R., & Miller, D. (2011). Energy failure in multiple sclerosis and its investigation using MR techniques. *Journal of Neurology*, *258*(12), 2113–2127. https://doi.org/10.1007/s00415-011-6117-7

Petroff, O. A. C., Errante, L. D., Kim, J. H., & Spencer, D. D. (2003). N-acetyl-aspartate, total creatine, and myo-inositol in the epileptogenic human hippocampus. *Neurology*, *60*(10), 1646–1651. https://doi.org/10.1212/01.WNL.0000068020.85450.8B

Pike, M. M., Frazer, J. C., Dedrick, D. F., Ingwall, J. S., Allen, P. D., Springer, C. S., & Smith, T. W. (1985). 23Na and 39K nuclear magnetic resonance studies of perfused rat hearts. Discrimination of intra- and extracellular ions using a shift reagent. *Biophysical Journal*, *48*(1), 159–173. https://doi.org/10.1016/S0006-3495(85)83769-3

Rajan, J., Poot, D., Junta, J., & Sijbers, J. (2010). Noise measurement from magnitude MRI using local estimates of variance and skewness. *Physics in Medicine and Biology*, *55*(22), 6973. https://doi.org/10.1088/0031-9155/55/22/6973

Reetz, K., Romanzetti, S., Dogan, I., Saß, C., Werner, C. J., Schiefer, J., Schulz, J. B., & Shah, N. J. (2012). Increased brain tissue sodium concentration in Huntington's disease—A sodium imaging study at 4T. *NeuroImage*, *63*(1), 517–524. https://doi.org/10.1016/j.neuroimage.2012.07.009

Ridley, B., Marchi, A., Wirsich, J., Soulier, E., Confort-Gouny, S., Schad, L., Bartolomei, F., Ranjeva, J.-P., Guye, M., & Zaaraoui, W. (2017). Brain sodium MRI in human epilepsy: Disturbances of ionic homeostasis reflect the organization of pathological regions. *NeuroImage*, *157*, 173–183. https://doi.org/10.1016/j.neuroimage.2017.06.011

Ridley, B., Nagel, A. M., Bydder, M., Maarouf, A., Stellmann, J.-P., Gherib, S., Verneuil, J., Viout, P., Guye, M., Ranjeva, J.-P., & Zaaraoui, W. (2018). Distribution of brain sodium long and short relaxation times and concentrations: A multi-echo ultra-high field 23Na MRI study. *Scientific Reports*, *8*(1), 4357. https://doi.org/10.1038/s41598-018-22711-0

Ridley, B., Wirsich, J., Bettus, G., Rodionov, R., Murta, T., Chaudhary, U., Carmichael, D., Thornton, R., Vulliemoz, S., McEvoy, A., Wendling, F., Bartolomei, F., Ranjeva, J.-P., Lemieux, L., & Guye, M. (2017). Simultaneous intracranial EEG-fMRI shows inter-modality correlation in time-resolved connectivity within Normal areas but not within epileptic regions. *Brain Topography*, *30*(5), 639–655. https://doi.org/10.1007/s10548-017-0551-5

Rooney, W. D., & Springer, C. S. (1991). A comprehensive approach to the analysis and interpretation of the resonances of spins 3/2 from living systems. *NMR in Biomedicine*, *4*(5), 209–226. https://doi.org/10.1002/nbm.1940040502

Rose, C. R., & Karus, C. (2013). Two sides of the same coin: Sodium homeostasis and signaling in astrocytes under physiological and pathophysiological conditions: Sodium homeostasis in astrocytes. *Glia*, *61*(8), 1191–1205. https://doi.org/10.1002/glia.22492

Seabold, S., & Perktold, J. (2010). Statsmodels: Econometric and statistical modeling with python. Proceedings of the 9th Python in Science Conference.

Seifert, G., & Steinhäuser, C. (2013). Neuron–astrocyte signaling and epilepsy. *Experimental Neurology*, *244*, 4–10. https://doi.org/10.1016/j.expneurol.2011.08.024

Simister, R. J., McLean, M. A., Barker, G. J., & Duncan, J. S. (2009). Proton MR spectroscopy of metabolite concentrations in temporal lobe epilepsy and effect of temporal lobe resection. *Epilepsy Research*, *83*(2), 168–176. https://doi.org/10.1016/j.eplepsyres.2008.11.006

Simister, R. J., Woermann, F. G., McLean, M. A., Bartlett, P. A., Barker, G. J., & Duncan, J. S. (2002). A short-echo-time proton magnetic resonance spectroscopic imaging study of temporal lobe epilepsy. *Epilepsia*, *43*(9), 1021–1031. https://doi.org/10.1046/j.1528-1157.2002.50701.x

Sofroniew, M. V., & Vinters, H. V. (2010). Astrocytes: Biology and pathology. *Acta Neuropathologica*, *119*(1), 7–35. https://doi.org/10.1007/s00401-009-0619-8

Statistical Parametric Mapping: The Analysis of Functional Brain Images—1st Edition. (n.d.). Retrieved November 3, 2021, from https://www.elsevier.com/books/statistical-parametric-mapping-the-analysis-of-functional-brain-images/penny/978-0-12-372560-8

Stefano, N. D., Matthews, P. M., Ford, B., Genge, A., Karpati, G., & Arnold, D. L. (1995). Short-term dichloroacetate treatment improves indices of cerebral metabolism in patients with mitochondrial disorders. *Neurology*, *45*(6), 1193–1198. https://doi.org/10.1212/WNL.45.6.1193

Stys, P., Waxman, S., & Ransom, B. (1992). Ionic mechanisms of anoxic injury in mammalian CNS white matter: Role of Na+ channels and Na(+)-Ca2+ exchanger. *The Journal of Neuroscience*, *12*(2), 430–439. https://doi.org/10.1523/JNEUROSCI.12-02-00430.1992

Urenjak, J., Williams, S. R., Gadian, D. G., & Noble, M. (1993). Proton nuclear magnetic resonance spectroscopy unambiguously identifies different neural cell types. *The Journal of Neuroscience: The Official Journal of the Society for Neuroscience*, *13*(3), 981–989.

Vagnozzi, R., Tavazzi, B., Signoretti, S., Amorini, A. M., Belli, A., Cimatti, M., Delfini, R., Di Pietro, V., Finocchiaro, A., & Lazzarino, G. (2007). Temporal window of metabolic BRAIN vulnerability to concussions. *Neurosurgery*, *61*(2), 379–389. https://doi.org/10.1227/01.NEU.0000280002.41696.D8

van der Hel, W. S., van Eijsden, P., Bos, I. W. M., de Graaf, R. A., Behar, K. L., van Nieuwenhuizen, O., de Graan, P. N. E., & Braun, K. P. J. (2013). *In vivo* MRS and histochemistry of status epilepticus-induced hippocampal pathology in a juvenile model of temporal lobe epilepsy. *NMR in Biomedicine*, *26*(2), 132–140. https://doi.org/10.1002/nbm.2828

Voets, N. L., Hodgetts, C. J., Sen, A., Adcock, J. E., & Emir, U. (2017). Hippocampal MRS and subfield volumetry at 7T detects dysfunction not specific to seizure focus. *Scientific Reports*, *7*(1), 16138. https://doi.org/10.1038/s41598-017-16046-5

Wang, Y.-H., An, Y., Fan, X.-T., Lu, J., Ren, L.-K., Wei, P.-H., Cui, B.-X., Du, J.-L., Lu, C., Wang, D., Zhang, H.-Q., Shan, Y.-Z., & Zhao, G.-G. (2018). Comparison between simultaneously acquired arterial spin labeling and 18F-FDG PET in mesial temporal lobe epilepsy assisted by a PET/MR system and SEEG. *NeuroImage Clinical*, *19*, 824–830. https://doi.org/10.1016/j.nicl.2018.06.008

Wang, Y., Majors, A., Najm, I., Xue, M., Comair, Y., Modic, M., & Ng, T. C. (1996). Postictal alteration of sodium content and apparent diffusion coefficient in epileptic rat brain induced by kainic acid. *Epilepsia*, *37*(10), 1000–1006. https://doi.org/10.1111/j.1528-1157.1996.tb00539.x

Waxman, S. G. (2006). Axonal conduction and injury in multiple sclerosis: The role of sodium channels. *Nature Reviews: Neuroscience*, *7*(12), 932–941. https://doi.org/10.1038/nrn2023

Zaaraoui, W., Konstandin, S., Audoin, B., Nagel, A. M., Rico, A., Malikova, I., Soulier, E., Viout, P., Confort-Gouny, S., Cozzone, P. J., Pelletier, J., Schad, L. R., & Ranjeva, J.-P. (2012). Distribution of brain sodium accumulation correlates with disability in multiple sclerosis: A cross-sectional 23Na MR imaging study. *Radiology*, *264*(3), 859–867. https://doi.org/10.1148/radiol.12112680

Zhao, H., Carney, K. E., Falgoust, L., Pan, J. W., Sun, D., & Zhang, Z. (2016). Emerging roles of Na+/H+ exchangers in epilepsy and developmental brain disorders. *Progress in Neurobiology*, *138–140*, 19–35. https://doi.org/10.1016/j.pneurobio.2016.02.002

SUPPORTING INFORMATION

Additional supporting information can be found online in the Supporting Information section at the end of this article.

How to cite this article: Azilinon, M., Makhalova, J., Zaaraoui, W., Medina Villalon, S., Viout, P., Roussel, T., El Mendili, M. M., Ridley, B., Ranjeva, J.-P., Bartolomei, F., Jirsa, V., & Guye, M. (2023). Combining sodium MRI, proton MR spectroscopic imaging, and intracerebral EEG in epilepsy. *Human Brain Mapping*, *44*(2), 825–840. https://doi.org/10.1002/hbm.26102